Heliyon 8 (2022) e12471

Contents lists available at ScienceDirect

Heliyon

journal homepage: www.cell.com/heliyon

Research article

Micro-CT analysis of osteomyelitis of rabbit tibial for model establishment and biomaterials application in tissue engineering

Yufan Li [a], Li Chen [b], Mingyue Lin [a], Chenxin Wang [a], Rui Zhang [a], Yubao Li [a,**], Qin Zou [a,*]

[a] Analytical and Testing Center, Nano Biomaterials Research Center, Sichuan University, No. 29 Jiuyanqiao Wangjiang Road, Chengdu, Sichuan, 610064, China
[b] Analytical and Testing Center, Sichuan University, No. 29 Jiuyanqiao Wangjiang Road, Chengdu, Sichuan, 610064, China

ARTICLE INFO

Keywords:
Osteomyelitis
Animal model
Micro-CT
Bone tissue engineering

ABSTRACT

Osteomyelitis is one of the most difficult diseases to treat in orthopedics field. The construction of animal models of osteomyelitis is now more mature but still lacks a deeper criterion other than "successful infection". In this work, rabbit tibial osteomyelitis model with *S. aureus* infection was established. Whole tibia, cortical bone around bone window, and tibial condyle were characterized in considerable detail using micro-CT and other means at 2/4/6 weeks, respectively. The results show that in addition to the obvious inflammatory response and bone destruction, osteomyelitis caused some other effects on compact and cancellous bone, and in particular, changes in bone mineral density after infection were of interest. Although the modeling groups all exhibited osteolysis and bone loss, their overall bone mineral density averages and those of the control groups were mostly in the range of 870 mg/cm^3 to 920 mg/cm^3, without statistical difference. The results suggest that overall bone mineral density is determined by both bone destruction conditions and the amount of dead bone deposition. This work provides a reference basis for the selection of time points for the subsequent animal models establishment and some valuable reference indicators of the application of biomaterials in tissue engineering.

1. Introduction

Osteomyelitis is an inflammatory condition characterized by bone damage that is caused by an invading bacterium [1]. *Staphylococcus aureus* (*S. aureus*) is currently the most predominant pathogen of osteomyelitis worldwide [2], which accounts for 80–90% of the causative germs that induce osteomyelitis infection [3]. During inflammation, the infection can be localized to a single area of the bone or spread to numerous regions, including the cortex, marrow cavity, periosteum, and soft tissue around it [4]. It may produce sinus tracts and dead cavities, and bone will gradually be damaged as well as surrounding soft tissues, which lead to osteophytes, osteoporosis, and the formation of sequestra (dead bones), making it a clinically difficult disease to treat at present [5]. After debridement, removal of dead bone, repair of bone defects, and supplemental antibiotic therapy are effective strategies for the treatment of osteomyelitis. New treatments for infected bone defects have advanced in recent years with the research of composite artificial bone replacement materials and biologic drug delivery systems [6]. Various treatment modalities such as drug-loaded nanoparticles [7], microwave-assisted bacterial killing [8], antimicrobial inorganic bone grafts [9], have driven the progress of osteomyelitis research. However, there are still many obstacles to the treatment of osteomyelitis. For example, the deposition of a large number of avascular sequestra (dead bones) will hinder the implementation of conventional antibiotic therapy [10]. Therefore, whether animal models can be constructed that can accurately mimic the patient's pathogenesis is vital to the treatment of osteomyelitis.

In order to better simulate the process of chronic osteomyelitis, understand its pathogenesis and investigate the effects of different treatments, it is important to establish stable and reproducible animal models of chronic osteomyelitis. Therefore, the construction of an osteomyelitis model with *S. aureus* as the causative agent is of great significance for bone tissue engineering. The earliest studies on the establishment of osteomyelitis models can be traced back to the work of Rodet in 1885 [11]. Later in 1941, the experiments of Scheman et al. [12] laid the foundation for the method of constructing animal models of osteomyelitis. Their research was further advanced until 1980 by Norden et al. [13]. Until today, more methods on the establishment of animal models of osteomyelitis are emerging. Nevertheless, few studies have pointed out that models with different levels of infection may have a significant impact on the evaluation of the effectiveness of biomaterials

* Corresponding author.
** Corresponding author.
E-mail addresses: nic7504@scu.edu.cn (Y. Li), zouqin80913@126.com (Q. Zou).

https://doi.org/10.1016/j.heliyon.2022.e12471
Received 3 April 2022; Received in revised form 8 July 2022; Accepted 12 December 2022

and drugs. With the relative maturity of modeling techniques today, perhaps the choice of treatment model should not be limited to the "success" of the infection.

The application of evolving imaging and histology techniques for evaluating bone infections in recent years has promoted a growing understanding of the pathogenesis of *S. aureus* osteomyelitis and has provided the basis for the application of multiple therapeutic approaches and detection assays in clinical treatment work. Micro Computed Tomography (micro-CT) is a non-destructive 3D imaging technique that allows clear visualization of the internal microstructure of a sample without destroying it. The resolution of it is extremely high, with a spatial resolution of 1–10 μm and even 0.25 μm in some advanced models [14]. Micro-CT is able to present 3D features and 2D sectional images of the bone areas of osteomyelitis lesions. Therefore, micro-CT is widely used for osteomyelitis modeling and the characterization of materials that promote osteogenesis in related bone tissue engineering. Based on previous animal models of osteomyelitis, most studies have been devoted to the reconstruction of bone defects after debridement or antibacterial treatment. However, early diagnosis and quantification of criteria for osteonecrosis and subsequent osteogenic activity during treatment are also directions for further research in the future. Changes in CT parameters are also instructive for later bone repair characterization [14]. For example, microstructure of trabeculae such as trabecular number (Tb. N), trabecular thickness (Tb. Th), and trabecular separation (Tb. Sp) can be calculated by the micro-CT analysis system. They are the main indicators for evaluating the spatial morphological structure of trabeculae and can respond to osteoporosis and osteomalacia. At present, more in-depth studies are still needed on how to establish more uniform quantitative criteria for bone repair in osteomyelitis. In previous animal models of osteomyelitis establishment, experimenters often focused more on whether the model was successfully established, but the specific differences in the severity of inflammation in different periods were usually not taken into account. Hence, it is of greater interest whether animal models with different levels of infection can be prepared at various time points to simulate the clinical patient status at different periods. This work expects to provide the specifics of damage in rabbit osteomyelitis models at different modeling time points with the assistance of micro-CT to provide a reference base for subsequent bone repair and antimicrobial studies.

In this experiment, rabbit tibiae infected by *S. aureus* after 2/4/6 weeks were characterized minutely by micro-CT. A detailed analysis of whole tibia, cortical bone around bone window, and tibial condyles was performed, respectively. It was found that the internal changes in bones varied greatly at different periods of infection which implies that precise choice of treatment timing after modeling is critical to avoiding potentially misleading assessment of the therapeutic effect of biomaterials.

2. Materials and methods

2.1. Materials

Staphylococcus aureus (*S. aureus*, CMCC(B) 26003) was purchased from Shanghai Bioresource Collection Center Co., Ltd (Shanghai, China). LB broth (HB 0128) was purchased from Hopebio Co., Ltd (Qingdao, China).

2.2. Inoculum preparation

The *S. aureus* bacterial count of every inoculum was verified by quantitative culture on Luria-broth (LB) agar (Figure 1b). The morphology of the *S. aureus* under SEM is shown in Figure 1c. A Single colony was picked and cultured in 2.5% Luria- LB cultures at 37 °C and 150 rpm/min for 8–16 h to get bacterial inoculum. A total of 1 mL bacterial solution was added to 100 mL LB cultures followed by growth at 37 °C and 150 rpm/min for 3–6 h. The inoculum size used in this study was 1×10^8 CFU per contamination. *S. aureus* was collected into syringes for later use.

2.3. Animal surgery

The establishment of chronic osteomyelitis model in 20 male New Zealand white (NZW) rabbits (2–3 kg) was mainly based on Horn and Norden's method [13, 15]. All surgical procedures were approved by the Ethics Committee of the West China Animal Experiment Center of Sichuan University. The experimental protocol was approved by the Sichuan Provincial Laboratory Animal Management Committee with approval number SYXK 2018-113, and the experimental procedure followed the International Association of Veterinary Medical Editors' "Consensus of Authors' Guide on Animal Ethics and Welfare" and local and national regulations.

The animals were randomly assigned to two separate surgical groups (a modeling group (n = 15) and a sterile saline normal group (n = 5). For the modeling group, the rabbits were anesthetized with 3% pentobarbital sodium. A longitudinal skin incision was made on the medial side of each proximal tibia to separate subcutaneous tissue and fascia. The periosteum was stripped to expose the medial and superior sides of the tibiae (Figure 1d). By sequential reaming, a 4-mm-wide defect was drilled by hand into the tibial lateral surface to open the tibial medullary canal. Subsequently, the tibial medullary cavity was flushed with sterile saline to remove bone fragments and hematoma. After sealing bone windows with bone wax (Figure 1e), sodium morrhuate (5 wt%, 0.1 mL) and *S. aureus* solution (1×10^8 CFU/mL, 0.1 mL) were injected into the medullary cavity in turn (Figure 1f). After insertion, the hole was sealed with bone wax. The wound was closed in layers with sutures. The sterile saline normal group was treated in the same way as the modeling group except for the injection of *S. aureus* and sodium morrhuate.

Five rabbits were randomly selected from the modeling group at 2/4/6 weeks respectively as shown in Table 1. After X-ray imaging, they were euthanized, and then their tibiae were taken for Micro-CT scanning. The right tibiae of rabbits sacrificed at 2W, 4W, 6W were defined as the 2W-M, 4W-M, 6W-M group respectively. Their contralateral tibiae were defined as the 2W-C, 4W-C, 6W-C group. It is particularly worth mentioning here that both control groups and sterile saline normal group were used to compare with the modeling groups.

2.4. Post-mortem bacterial culture

After the operation, daily activities frequency of the modeling group decreased significantly, and their gaits were halting. Local abscesses at knees were observed in 2 weeks, and purulent secretion could be found inside (Figure 2a). Some of the rabbits at the fourth week were found to have pus outflow from surgical sites (Figure 2b). This may indicate new bone formation in the internal necrotic area [16]. In 6 weeks, severe local festering happened, and sinus tracts emerged at some of surgical positions (Figure 2c).

After sacrifice, the tibiae were dissected aseptically. To assess soft tissue infection, purulent secretion taken from tibial lateral surface was evaluated for the presence of *S. aureus* on tellurite glycine agar plates. After 24 h, culture dishes were quantified for specific bacterial growth. It could be seen that a large number of bacteria were distributed on the plate (Figure 2d). SEM micrographs showed that abundant *S. aureus* was adhering to tissues, which revealed the success of modeling (Figure 2e, 2f).

2.5. X-ray images

Five rabbits from the modeling group were randomly taken for radiographs at 2/4/6 weeks, respectively, as well as the sterile saline normal group to detect bone tissue changes during the formation of rabbit tibial osteomyelitis model. Each rabbit was sacrificed for follow-up studies after being radiographed.

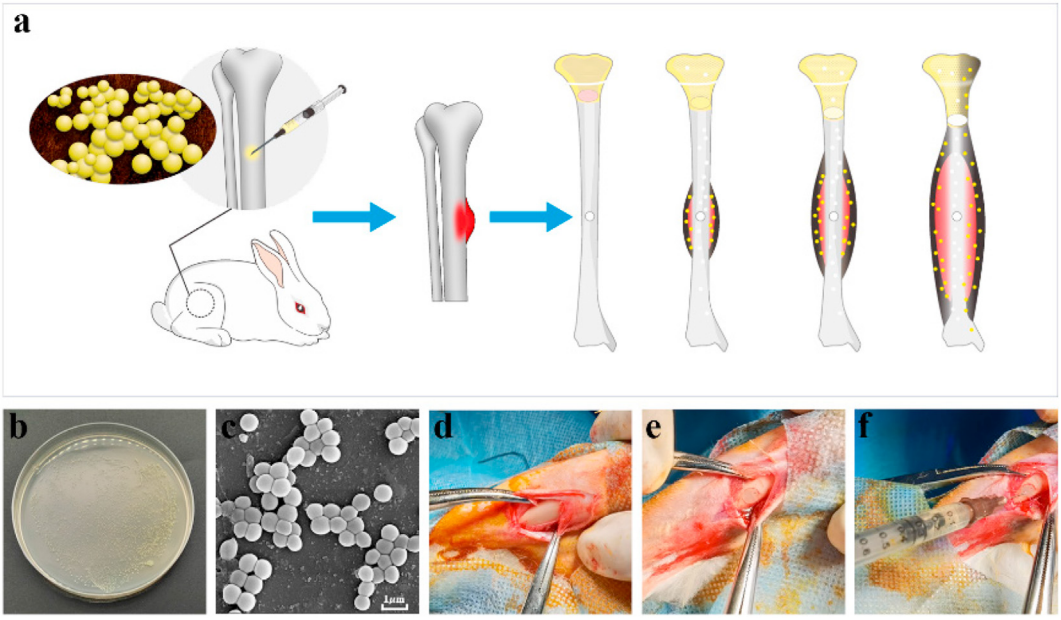

Figure 1. (a) *S. aureus* was injected into rabbit tibial medullary cavity to establish an animal model of osteomyelitis, and inflammation grows progressively worse over time. (b) *S. aureus* in agar plates after cultured for 24 h. (c) *S. aureus* used for injection under SEM. (d) Exposure of injection site. (e) Drilling of bone window and filled with bone wax. (f) Injection of *S. aureus* into the bone window.

Table 1. Grouping of the rabbits.

	Groups						
	Normal group (Sterile saline group) (n = 5)	Modeling group (Right tibiae) (n = 15)			Control group (Left tibiae) (n = 15)		
Time		2W-M (n = 5)	4W-M (n = 5)	6W-M (n = 5)	2W-C (n = 5)	4W-C (n = 5)	6W-C (n = 5)
2W	**X (did not sacrifice)**	**XSC**			**XSC**		
4W	**X (did not sacrifice)**		**XSC**			**XSC**	
6W	**XSC**			**XSC**			**XSC**

X: X-ray, **S**: sacrifice, **C**: Micro-CT.

2.6. Gross observation

After sacrifice, all tibiae were dissected aseptically and observed. Then, after decalcification, the tibia was dissected transversely or longitudinally and their epiphysis and diaphysis were observed in profile.

2.7. Micro-CT analysis

The rabbits were sacrificed and their tibiae were removed after the radiographs were taken. Then the tibiae of 2/4/6 weeks modeling groups and the control groups were scanned by Micro-CT (vivaCT80, SCANCO Medical AG, Switzerland). The scanning parameters were as follows: scanning voltage 70 kVp, current 114 μA, power 8 W, system resolution selected as medium resolution (scanning rotation 360°, acquisition of 1000 projection images), voxel size of 35 μm. The corresponding tomographic images were obtained and reconstructed in 3D. Through tomography scan, the morphological structure of trabeculae within condyles can be clearly visualized as well as the degree of cortical bone proliferation and lesions due to inflammation. 3D reconstruction not only provides a clear picture of the entire bone but also allows cutting at any place to observe a cross-section, which is easy to operate and intuitive.

The impact of osteomyelitis was evaluated from three aspects: the tibial condyle (cancellous bone), the diaphysis (cortical bone), and the whole tibia. In order to determine a criterion for Micro-CT characterization of the affected condition of the diaphysis, a range of 300 layers above and below the injected site of each sample (600 layers in total, about 2.1 cm) was selected as the region of interest (ROI) for characterization and comparison. By selecting the ROI, swollen areas can be extracted and analyzed separately [17]. For each sample, three tomographic images were taken at the bone window and its upper and lower 150 layers (about 5.25 mm) for comparative analysis of the cortical bone affected by osteomyelitis (Figure 3 dotted lines). The quantitative analysis is based on the 3D reconstruction of the ROI, and these 3 images are mainly used for demonstration. The entire epiphysis above epiphyseal line and metaphysis below it were selected as the ROI to analyze the changes in trabeculae within the tibial condyles subjected to osteomyelitis. The portion that begins at the epiphyseal line and ends at the most distal point to which the cancellous bone extends was considered as metaphysis. For each sample, three tomographic images were taken within epiphysis above epiphyseal line, at the junction of epiphysis and metaphysis, and at the metaphysis to analyze the effect of osteomyelitis on cancellous bone (Figure 3 dotted lines). The "SCANO μCT Evaluation Program" software was used to calculate the relevant bone parameters such as bone mineral density (BMD) and bone volume (BV) for each group of samples, and those with significant changes were selected for comparative analysis. Whole tibia, cortical bone around the bone window and tibial condyle were included in the comparative analysis.

BV is an important value of bone morphology, which measures the development of bone and is also closely related to the mechanical properties of bone. In this experiment, the changes in BV mainly reflected the swelling of bone after being affected by osteomyelitis. BMD is an index that describes the mineral content of bone tissue, reflects the degree of osteoporosis, and predicts the risk of fracture [18, 19]. The BMD is measured by the X-ray attenuation principle of Micro-CT to obtain the equivalent density of hydroxyapatite (HA) accurately converted from the

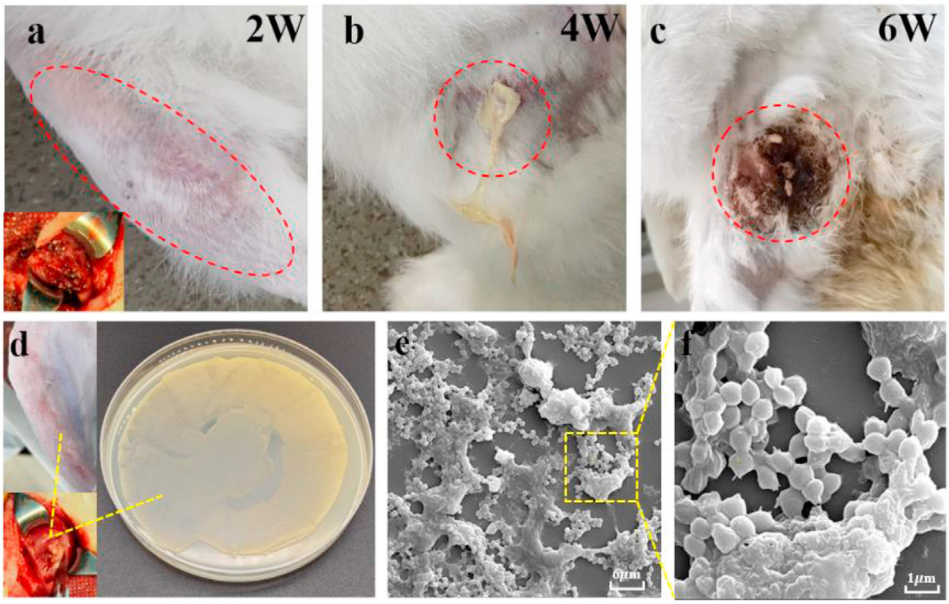

Figure 2. (a) Local abscesses and purulent secretion in 2 weeks. (b) Pus outflow from surgical sites at the fourth week. (c) Sinus tract at the surgical position. (d) Purulent secretion was extracted and cultured on plates. A large number of bacteria can be observed on the plate. (e) SEM micrograph of bacterial in purulent secretion at 2000×. (f) SEM micrograph of bacterial in purulent secretion at 10000×.

CT value of the scanned image. A phantom has been used to calibrate before the measurements. The BMD in the paper refers to the BMD of the bone and does not include air. Large areas of pore space will not be included in the BMD measurement results.

2.8. Statistical analysis

Independent samples t-test was used for comparison among the groups at different time points, and paired t-test was used for the control and modeling groups at the same time point. The statistical analysis was performed using Excel's T.TEST function. Differences were statistically significant when $P < 0.05$.

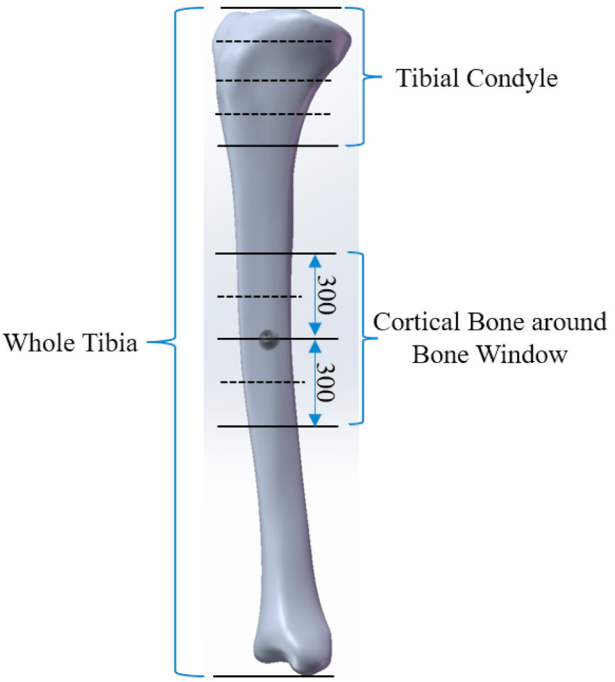

Figure 3. Schematic diagram of the sites analyzed and calculated by micro-CT.

3. Results

3.1. Whole tibia

Comparing control groups at 2/4/6 weeks by gross observation (Figure 4e), bone volume increased slightly. Average values were 1905.82 ± 176.47 mm^3, 1997.84 ± 183.96 mm^3 and 2311.17 ± 126.18 mm^3 respectively according to Figure 4g. The bone surface was smooth and flat without abnormal proliferative bone (Figure 4e). Under X-ray evaluation, it could be observed that the normal group had good bone continuity and complete bone cortex (Figure 4a) while the 2W-M group had slight hyperosteogeny and periosteal reaction around the modeling position (Figure 4b), which was the basic symptom of bone lesions [20]. Obvious swelling along the whole tibia did not seem to appear (Figure 4b). However, the analysis results of micro-CT showed that compared with the 2W-C group, the average volume of the modeling group increased by 21.87% ($p < 0.05$) (Figure 4g), which could not be significantly found in the X-ray and gross observation image results. In addition, the micro-CT 3D reconstructions showed significant lysis and destruction of the internal cancellous bone and hyperplasia along the medullary cavity toward the distal tibia (Figure 4f, 2W-M circled), and the cortical bone was thickened compared to the control group (Figure 4f 2W-M arrowed), which provides an important reference for the determination of the pre-inflammation severity. At 4 weeks, the periosteal reaction exacerbated according to the X-ray (Figure 4c). In addition, tibial lateral surface deformed locally and an aberrant mass could be found above the modeling position (Figure 4e, 4W-M). The overall BV increased by approximately 39.21% compared to the control group ($p < 0.01$). The reconstructed section shows severe endosteal destruction and obvious thickening of the cortical bone around the molded position (Figure 4f, 4W-M arrowed). More serious, grievous swelling happened apparently at 6 weeks accompanied by fierce periosteal reaction (Figures 4d,4e). On X-ray films, a progressive increase in sequestrum formation and periosteal reaction, as well as inhomogeneous osteosclerosis can be seen (Figure 4d), which were the hallmark features of chronic osteomyelitis on plain radiographs [4, 21, 22]. The cross-section shows marked endosteal destruction, disorganized trabeculae, and increased cortical porosity (Figure 4f, 6W-M). At the same time, rim osteosclerosis with large areas of sequestra forming around the original bone

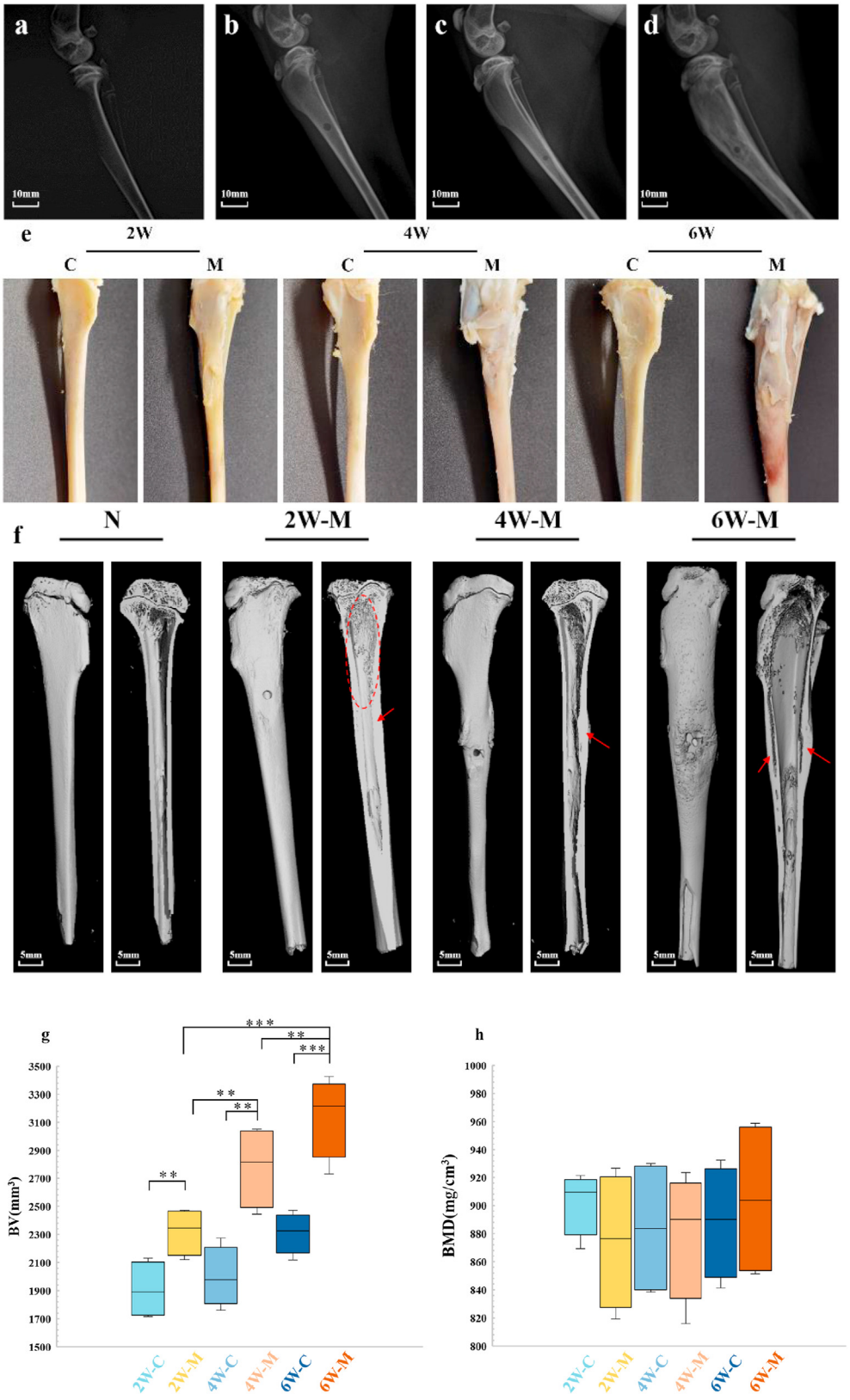

Figure 4. (a,b,c,d) X-ray films of normal group, 2W, 4W, and 6W modeling group respectively. (e) Gross observation of 2W, 4W, 6W control and modeling groups respectively. C represents control and M represents modeling. (f) 3D reconstruction of normal group, 2W, 4W, and 6W modeling group and their cross-section respectively. (g) Whole tibia volume of control groups and modeling groups at 2W, 4W, 6W respectively. (h) Whole tibia bone mineral density of control groups and modeling groups at 2W, 4W, 6W respectively. $P^* < 0.05$, $P^{**} < 0.01$.

(Figure 4f, 6W-M arrowed). These symptoms are difficult to visualize on radiographs (Figure 4d). According to micro-CT bone composition analysis, the most severely swollen tibia and its contralateral tibia had volumes of 3425.89 mm^3 and 2308.02 mm^3, respectively, with a growth rate of 48.43% (Figure 4g). Progressively worsening osteolysis of metaphyseal and diaphyseal in each group indicated increased inflammation [23].

Interestingly, no statistical difference was seen in overall tibial BMD from 2 to 6 weeks (Figure 4h). A vast majority of bones had densities between 870 mg/cm^3 and 920 mg/cm^3, albeit some modeling groups

showing abnormally high or low values (e.g., as low as 815.98 mg/cm^3 at 4 weeks and as high as 958.57 mg/cm^3 at 6 weeks) (Figure 4h). However, this does not indicate that there is no significant change in bone structure, which is clearly repugnant to the image results. The causes of this phenomenon need to be considered in conjunction with subsequent separate analyses of cancellous and cortical bone.

3.2. Cortical bone around bone window

As seen by micro-CT tomographic images, the normal cortical bones of tibiae were morphologically intact and indiscrete (Figure 5, ①②③-N). Besides, 3D reconstruction clearly showed the degree of bone destruction and proliferation in each experimental group (Figure 5b). A gross cross-sectional view of the cortical bone shows that the marrow cavity of normal bone has a healthy blood-red color (Figure 5a, N). In the 2W-M group, bone was only slightly swollen at 2 weeks and no statistical significance was attained in BV quantitative analysis (Figure 5d). Increased cortical porosity was evident at the bone window and the upper part of it. Localized cavities appeared in cortical bones and osteolysis occurred (Figure 5, ①②-2W). The marrow cavity turns an unhealthy yellow color (Figure 5c, 2W), which means that its hematopoietic function is significantly affected. According to the 4W-M group, there was significant osseous expansion in cortical bone around the surgical area. Bone destruction and sclerosis can be found both above and below the surgical area (Figure 5, ②③-4W). There is no clear boundary between dead and living bone (Figure 5, c-4W). Above the surgical site, lamellar bone was

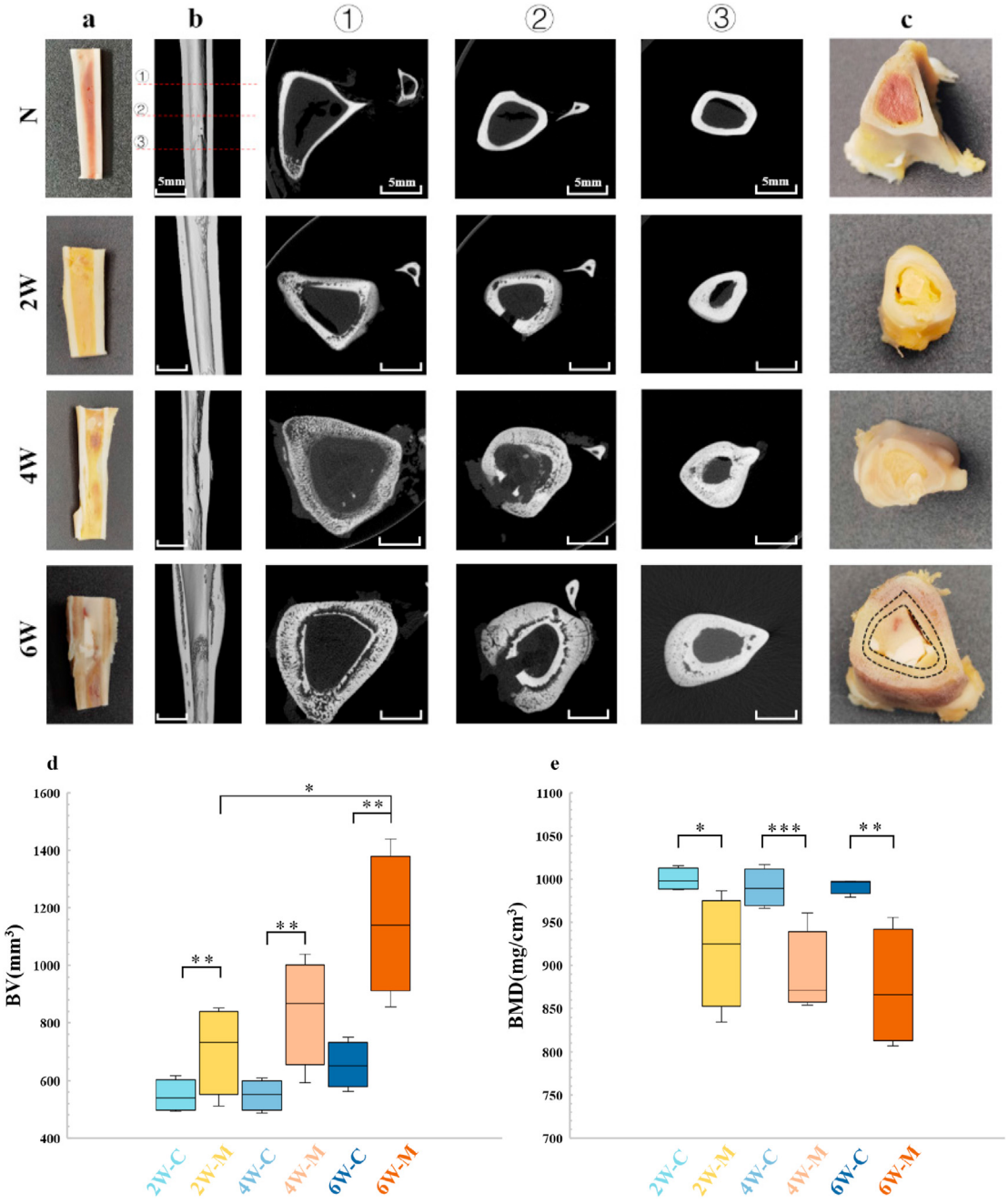

Figure 5. (a) The coronal sections of tibial diaphysis by gross observation. (b) The coronal sections of tibial diaphysis by micro-CT 3D reconstruction. (c) The transverse sections of tibial diaphysis by gross observation. ①②③ represent the transverse sections of each group above the modeling site, at the modeling site, and below the modeling site respectively by micro-CT, as shown in figure (N-b). (d) Whole cortical bone volume of control groups and modeling groups at 2W, 4W, 6W respectively. (e) Whole cortical bone mineral density of control groups and modeling groups at 2W, 4W, 6W respectively. $P^* < 0.05$, $P^{**} < 0.01$, $P^{***} < 0.001$.

dramatically sparse, and perhaps new woven bone was formed [24] (Figure 5, ①-4W). In the 6W-M group, the inflammation steadily deteriorated. Remodeling and resorption of the tibial cortex gradually intensify. Bone destruction, increased cortical porosity, and osseous expansion continued to aggravate, and conspicuous sequestrum could be seen around the original cortical bone (Figure 5, 6W). The boundary between dead and original bone becomes very distinct (Figure 5c, 6W), with extensive whitening of medullary cavity, suggesting a massive apoptotic and inflammatory response. Composition analysis showed an apparent volume increase in cortical bones at the modeling sites. Particularly, in the 4W-M and 6W-M groups compared to the control groups, cortical BV increased about 53.13% (from 549.60 mm^3 to 841.58 mm^3, $p < 0.05$) and 74.87% (from 653.93 mm^3 to 1143.51 mm^3, $p < 0.01$) respectively (Figure 5d).

The BMD of compact bone was obviously lower at 2/4/6 weeks compared to the control group, which implies that bone destruction caused by osteomyelitis resulted in severe bone loss. Besides, it may also related to the proliferation of new primary spongiosa. It is noteworthy that the variance of compact bone BMD was smaller in control groups, whereas the difference between samples was larger in modeling groups (Figure 5e). The mean compact bone BMD in the control group was around 994.11 ± 4.17 mg/cm^3, while the maximum value in the 2W-M group was 940.70 mg/cm^3 and the minimum value was 834.10 mg/cm^3 (Figure 5e). This can be interpreted as individual differences in the degree of inflammatory infection in different rabbits in the pre-osteomyelitis period. In the 6W-M group, however, all subjects already had a significant inflammatory condition, which cannot be simply interpreted as individual differences in the severity of inflammation. At this time, the maximum BMD was 955.97 mg/cm^3 and the minimum was 806.43 mg/cm^3 (Figure 5e). Such differences may be modulated by the amount of sequestra deposition and the severity of bone destruction. Remnants of dead bone lead to increased BMD while osteolytic damage and bone loss (increased cortical porosity) due to osteomyelitis lead to decreased BMD. The combination of the severity of the two factors determines the final BMD. Therefore, subject to individual differences, some subjects with low BMD of cortical bone may have experienced more severe osteolysis and bone destruction with small amount of sequestra, while subjects with high BMD deposited more sequestra, which has exceeded the volume of original bone (e.g. Figure 5, 6W).

3.3. Tibial condyle

For the normal group, as shown in micro-CT tomographic images, cancellous bones in epiphysis were homogeneous, and the trabecular structure was continuous with uniform thickness distribution, showing a regular spongy reticular structure (Figure 6, ①②③-N). There were also a few trabeculae in metaphysis (Figure 6b, N). In the 2W-M group, there was some hyperplasia of cancellous bones within metaphysis (Figure 6b, 2W). A few bone trabeculae were broken and lost their inherent continuity, and osteolysis was evident (Figure 6, 2W). The destruction of trabeculae in epiphysis and metaphysis was apparently more severe in the 4W-M group than in the 2W-M group. Cortical bone thickening was apparent at metaphysis and adjacent diaphysis (Figure 6a, 4W). According to the 6W-M group, trabeculae were seriously damaged, fractured, and deformed, and epiphyseal line was no longer noticeable (Figure 6b, 6W). The gross observation showed that the inflammatory reaction and bone proliferation increased with time (Figure 6a, 6c).

The micro-CT analysis result of the impact of osteomyelitis on cancellous bone is noteworthy. Bone trabeculae had been considerably disrupted as seen by tomographic images, then there was a predictable decrease in trabecular BMD due to bone destruction caused by osteomyelitis in the 4W-M and 6W-M group, which decreased by 11.47% and 16.07% respectively (Figure 6e, 6f). Tb. N represents the average number of intersections between bone and non-bone tissue per mm, which can be used to reflect the distribution density of bone trabeculae within tibia condyle. At 2/4/6 weeks, Tb.N decreased by 28.31%, 55.47% ($p < 0.01$), and 61.20% ($p < 0.001$), respectively (Figure 6d, 6e, 6f). Such a result is consistent with the symptom of bone destruction in cross-sectional views. In addition, the reduction of Tb. Th as well as the expansion of Tb. Sp was all predictable evidence of severe destruction of bone trabeculae. Tb. Th indicates the average thickness of bone trabeculae and Tb. Sp represents the average width of medullary cavity between bone trabeculae. When bone destruction occurs, Tb. Th and Tb. N decrease and Tb. Sp increases, suggesting an increase in bone resorption. The reduction of TB. Th in the 6W-M group was 44.28% ($p < 0.05$), while the increase of Tb.Sp reached an incredible 120.38% ($p < 0.01$) (Figure 6f). What should be of concern is that composition analysis revealed that a statistically significant increase in trabecular BV occurred in the modeling groups compared to the control groups (an increase of 61.87%, 44.93%, and 35.46%, respectively ($p < 0.01$)) (Figure 6d, 6e, 6f). This phenomenon can be corroborated by the results of 3D reconstruction. Bone trabeculae were destroyed while massive hyperplasia occurred and tended to spread to distal tibia (Figure 6b). Besides, as seen from the data, the amount of Tb.BV growth at 2/4/6 weeks gradually decreased compared to the control groups, while it remained almost constant (4W-M and 6W-M groups showed an increase in Tb. BV of 4.41% and 2.66% respectively, compared to the 2W-M group.) among modeling groups (Figure 6g). This may indicate that in the pre-osteomyelitis period, cells were stimulated by inflammation to proliferate vigorously to form a large number of bone trabeculae. In contrast, in the late stage of infection, the original process of bone resorption and formation has been seriously disrupted, then the trabecular BV was maintained at the same condition as at 2W. Further, at 4/6 weeks, a progressive decrease of Tb. N and Tb. Th and a gradual increase of Tb. Sp compared to the 2W-M group implied the persistent destruction of bone by osteomyelitis.

4. Discussion

4.1. The influence on BMD

In previous animal models of osteomyelitis, the inflammation of bone and its surrounding soft tissues was often characterized by bacterial cultures, X-rays, CT, and pathological tissue sections to demonstrate the success of osteomyelitis model construction. In this experiment, as far as we had observed, persistent bacteria, formation of fistulous tracts, pus, sequestra, and periosteal reaction were all distinct phenomena of chronic osteomyelitis [25], which indicated the success of modeling. However, although the graphical characterization of animal osteomyelitis models has been studied considerably in previous research, the specific changes numerically of compact and cancellous bone have rarely been analyzed in detail. Changes in local bone density and various parameters of bone trabeculae are essential for the study of animal models of osteomyelitis. This helps to provide a reference for the effectiveness of later osteomyelitis treatment.

One of the most notable data in this experiment was the change in BMD. Osteolysis and destruction of lamellar bone are to be expected. Osteolysis and bone destruction, as well as proliferation of new primary spongiosa can all reduce the value of BMD. Nevertheless, when the overall tibial BMD was calculated by micro-CT analytical systems, the BMD of modeling groups was found to be not statistically different from the control groups. This may be due to the fact that infected osteomyelitis bones develop osteoporosis along with the production of large amounts of sequestra, which represents necrotic bone that is denser than living bone [16]. After mutual neutralization of high-density sequestra and sparse living bone, the difference in average BMD from the control group may not have been noticeable. Therefore, in later drug-loaded bone repair experiments, the success of the inflammatory treatment cannot be proven solely from the insignificant difference of overall tibial BMD among groups. The anti-inflammatory effectiveness should be illustrated by separate analysis of BMD at different sites and supplemented with images together.

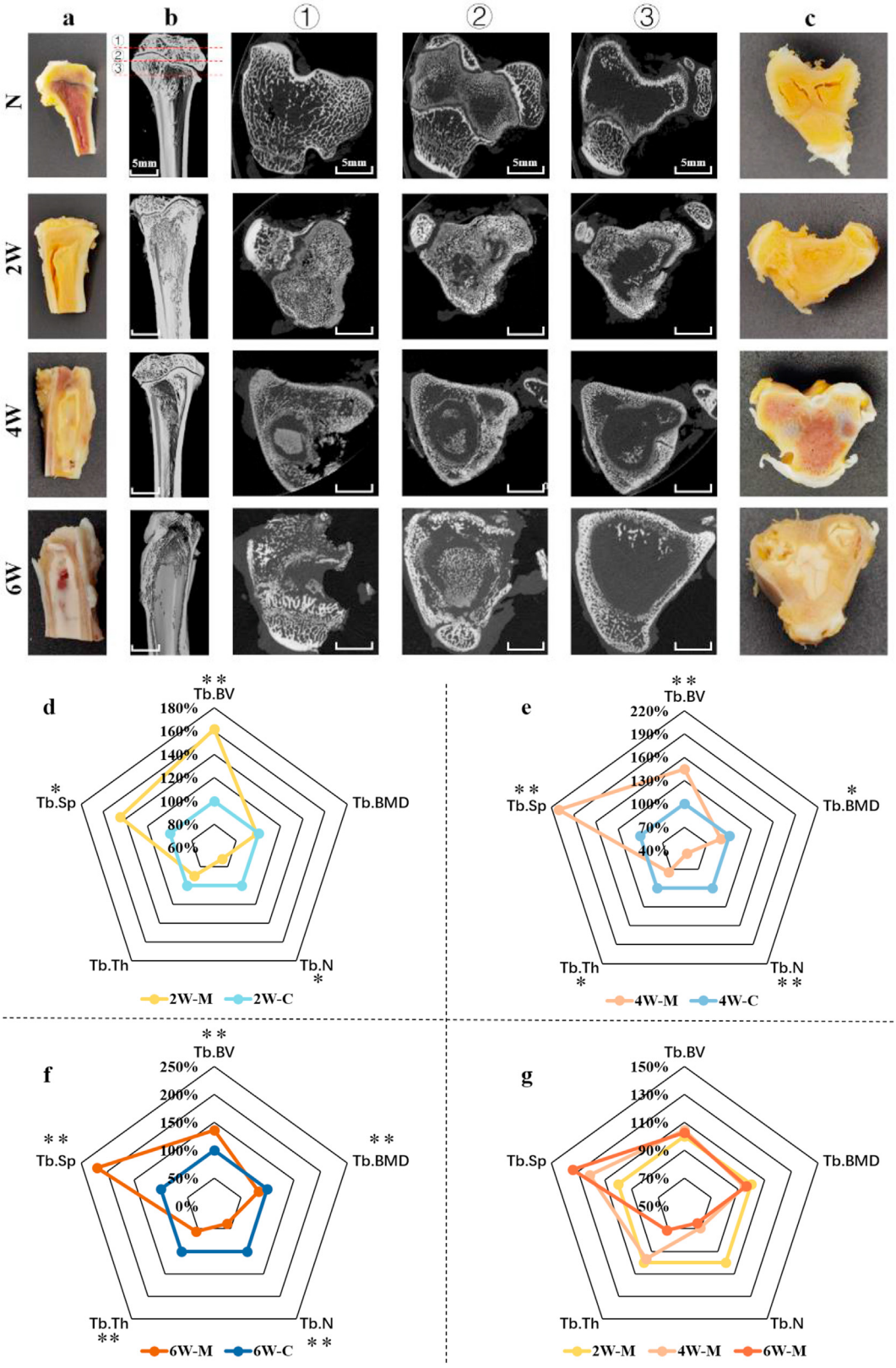

Figure 6. (a) The coronal sections of tibial condyle by gross observation. (b) The coronal sections of tibial condyle by micro-CT 3D reconstruction. (c) The transverse sections of tibial condyle by gross observation. ①②③ represent the transverse sections of each group above the modeling site, at the modeling site, and below the modeling site respectively by micro-CT, as shown in figure (N-b). (d,e,f) Comparison of trabecular structural parameters between modeling and control groups in 2W, 4W, and 6W respectively. (g) Comparison of trabecular structural parameters among each modeling group. $P^{*}<0.05$, $P^{**}<0.01$, $P^{***}<0.001$.Trabecular structural parameters including Tb.BV, Tb.BMD, trabecular separation (Tb. Sp), trabecular thickness (Tb. Th), and trabecular number (Tb. N).

4.2. The influence on BV

In this experiment, the increase in BV was mainly caused by two factors: post-inflammatory bone swelling and sequestra deposition. Although the rabbits may have increased in volume during the 6 weeks, the contralateral tibia of each sample was chosen as a control group to assess the impact of this phenomenon on the experiment. The results showed that the growth of the rabbits themselves at 2/4/6W was much less than the effect of osteomyelitis on them, with statistically significant differences between the groups.

In the later stages of osteomyelitis, dead bone covers almost the entirety of the original living bone (Figure 7d). The ability to effectively remove sequestrum becomes a key factor in the treatment of chronic osteomyelitis. Bone necrosis might be caused by ischemia due to the obliteration of vascular channels which made bones devoid of blood supply [4]. Sequestra were formed by the separation of these ischemic bone segments. As a result, an avascular area inaccessible to antibiotics and inflammatory cells formed and provided a good environment for continued bacterial growth [26]. Therefore, systemic administration of drugs to patients after being infected by osteomyelitis and the formation of large amounts of sequestra is hardly effective. This is the reason why most experiments choose to implant antimicrobial materials while molding to verify the anti-inflammatory ability of their materials [27, 28]. Achieving antimicrobial properties of a material is easy in the early stages of bacterial infection of bone, and treatment becomes more difficult as the infection grows longer. Qayoom et al. designed a drug-loaded bioceramic system that provides local and sustained delivery ability. It was able to completely eradicate pathogens from bone nidus even after three weeks of infection with osteomyelitis [29]. S. Zhang et al. designed a kind of vancomycin-loaded oligochitosan nanoparticles (Van-NPs) combined with PLGA-PEG-PLGA gel to cure osteomyelitis after two weeks of tibial infection in rats [30]. Nevertheless, there are seldom reports of recovery of osteomyelitis infections of six weeks or more. This may be the reason why long-term chronic osteomyelitis in clinical practice has been so arduous to cure so far. As in the 6W-M group in this experiment, trying to treat by targeted drugs sustained-release therapy becomes quite difficult after the apparent separation of dead and living bone. Drugs, immune cells, and blood have been completely blocked by sequestrum. Therefore, using imaging and analysis capabilities of micro-CT to follow the efficacy of affected limbs may help to achieve long-term chronic osteomyelitis recovery. And in addition to physical debridement, chemotherapy with more continuous treatment of sequestrum is of great research interest.

4.3. The influence on cancellous bone

In the analysis of cancellous bone, increased cortical porosity was accompanied by a downward growth of bone in metaphysis. Therefore, the decrease in trabecular density, which was also associated by proliferation of new primary spongiosa, and the increase in its volume within condyles were not in conflict, but rather due to the occurrence of bone destruction and osteolysis while osteoblasts were stimulated to induce the production of new bone [31]. Simultaneously, *S. aureus* infection causes the release of proinflammatory cytokines, which contributes to an increase in osteoclast resorption capacity [32]. Furthermore, as a result of the interaction between osteoclasts and *S. aureus*, inflammatory cells are recruited towards the bone, causing bone resorption [33]. The solubilization of bone mineral occurs in osteoclasts, which have acidified vesicles and chloride channels. Then cathepsin K can break down the bone matrix once it has been solubilized [34]. Consequently, the balance between osteoblasts and osteoclasts was disturbed by infection, and the original process of bone formation and reconstruction transformed into a phenomenon of massive bone destruction and proliferation [35, 36].

4.4. The influence on marrow cavity

As can be noted in previous sections, the color of marrow cavity varies in different modeling periods (as shown in Figure 7). In the 2W-M group, the medullary cavity changed from red to yellow, indicating that osteomyelitis inhibited the hematopoietic function within bones (Figure 7b). Osteomyelitis leads to apoptosis of bone cells and hematopoietic cells, and the resulting damage to blood flow is a precursor to the formation of sequestrum [37]. After the blockage of blood flow, bone resorption and formation procedure was also affected, and the original bone remodeling process is transformed into a process of living bone lysis and dead bone deposition [38]. More serious, gross observation showed extensive whitening of the medullary cavity in the 6W-M group, implying a severe inflammatory reaction. The inflammatory reaction in medullary cavity may develop as a result of a subperiosteal abscess entering the cavity via perforating or central canals, which infects vasa vasorum and their branches in medullary cavity. Thrombosis and embolism in blood vessels accelerated the onset of localized osteonecrosis. In parallel with suppuration and sequestrum formation, the periosteum surrounding the lesion was stimulated by inflammatory congestion and exudate to produce new bone that surrounds the original diaphysis. As the inflammation continues, new bone itself was destroyed, resulting in irregularities in lamellar bone and the formation of numerous foramina. These canals penetrated subcutaneous tissue and skin, forming sinus tracts.

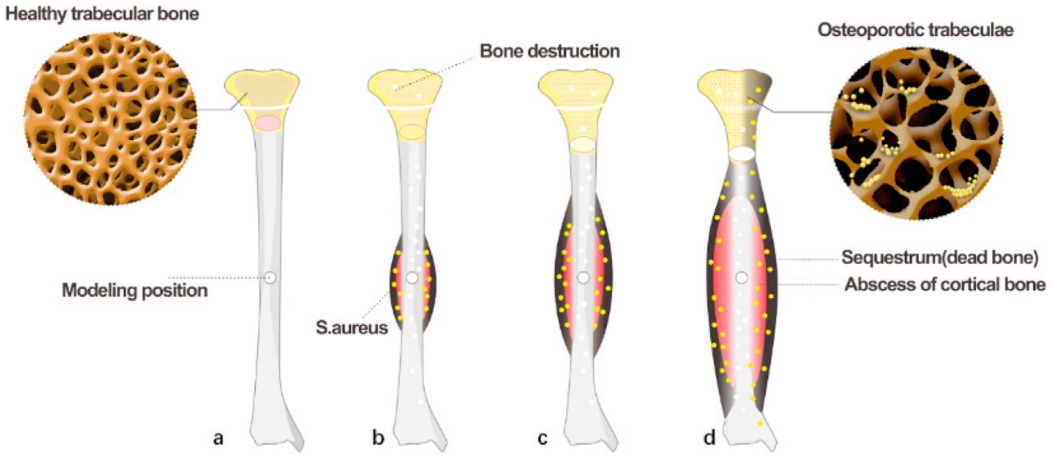

Figure 7. The diagram illustrates the changes of rabbit tibiae before and 2/4/6 weeks after the injection of bacteria. (a) represents the normal bone before modeling and (b, c, d) represent the bone modeled at 2,4,6 weeks, respectively. After modeling, bacteria adhere to the surface of lamellar bone, and the infected bone showed osteoporosis and osteolysis.

5. Conclusion

In this experiment, the establishment of *S. aureus* osteomyelitis in rabbit tibia was characterized by micro-CT evaluation and compared with gross observation and X-ray film. The greatest advantage of micro-CT is its continuity and integrity, which allows for clear visualization of changes in morphological structure of trabeculae within bone condyles due to inflammation, as well as cortical proliferation and detailed changes in bone parameters such as BV, BMD et al. through nondestructive cross-sectional imaging. The experiment showed that in the 2W-M group, there was a large amount of cancellous bone proliferation in tibial condyles and bone loss (increased cortical porosity) in cortical bone, and sequestra were not obvious (Figure 7b). In the 4W-M group, the destruction increased and the osteolysis and bone loss became more serious, and the boundary between dead and living bone was not clear enough (Figure 7c). In the 6W-M group, distinct separation of dead and living bone has been clearly observed. Such phenomena facilitate the establishment of animal models in the future. Experimenters can target animal models with different levels of infection according to the design of their own materials and drugs (Figure 7d). For example, to verify that a drug release system can still have an anti-inflammatory and restorative effect in advanced stages of chronic osteomyelitis where sequestrum has been heavily deposited, experiments on rabbits modeled over 6 weeks may be required to be convincing. On the other hand, a drug that has no apparent effect in late-stage cannot be simply dismissed. Perhaps it could have a remarkable effect on early osteomyelitis. The experiment will provides a reference for the application of *S. aureus* osteomyelitis animal models in biaomaterials design in tissue engineering.

Declarations

Author contribution statement

Yufan Li: Conceived and designed the experiments; Performed the experiments; Analyzed and interpreted the data; Wrote the paper.

Li Chen: Analyzed and interpreted the data; Contributed reagents, materials, analysis tools or data.

Mingyue Lin; Chenxin Wang; Rui Zhang: Performed the experiments.

Yubao Li: Conceived and designed the experiments.

Qin Zou: Conceived and designed the experiments; Performed the experiments; Analyzed and interpreted the data.

Funding statement

Yubao Li was supported by China NSFC project [32171338].

Dr. Qin Zou was supported by Key Science and Technology Special Project of Sichuan Province [2020ZDZX0008].

Data availability statement

Data will be made available on request.

Declaration of interest's statement

The authors declare no conflict of interest.

Additional information

No additional information is available for this paper.

Acknowledgements

We would like to thank Yi He at the Analytical & Testing Center of Sichuan University for his help with SEM analysis.

References

[1] D.P. Lew, F.A. Waldvogel, Osteomyelitis, New Engl. J. Med. 337 (6) (1997) 428–429.
[2] J. Yang, J.-L. Yao, Z.-Q. Wu, D.-L. Zeng, L.-Y. Zheng, D. Chen, Z.-D. Guo, L. Peng, Current opinions on the mechanism, classification, imaging diagnosis and treatment of post-traumatic osteomyelitis, Chin. J. Traumatol. 24 (6) (2021) 320–327.
[3] M. Monaco, F. Pimentel de Araujo, M. Cruciani, E.M. Coccia, A. Pantosti, Worldwide epidemiology and antibiotic resistance of Staphylococcus aureus, in: F. Bagnoli, R. Rappuoli, G. Grandi (Eds.), Staphylococcus aureus: Microbiology, Pathology, Immunology, Therapy and Prophylaxis, Springer International Publishing, Cham, 2017, pp. 21–56.
[4] D.P. Lew, F.A. Waldvogel, Osteomyelitis, Lancet 364 (9431) (2004) 369–379.
[5] Ciampolini, Pathophysiology of chronic bacterial osteomyelitis. Why do antibiotics fail so often? Postgrad. Med. 76 (898) (2000) 479–483.
[6] T. Garg, A.K. Goyal, Biomaterial-based scaffolds – current status and future directions, Expet Opin. Drug Deliv. 11 (5) (2014) 767–789.
[7] N. Hassani Besheli, F. Mottaghitalab, M. Eslami, M. Gholami, S.C. Kundu, D.L. Kaplan, M. Farokhi, Sustainable release of vancomycin from silk fibroin nanoparticles for treating severe bone infection in rat tibia osteomyelitis model, ACS Appl. Mater. Interfaces 9 (6) (2017) 5128–5138.
[8] Y. Qiao, X. Liu, B. Li, Y. Han, S. Wu, Treatment of MRSA-infected osteomyelitis using bacterial capturing, magnetically targeted composites with microwave-assisted bacterial killing, Nat. Commun. 11 (1) (2020) 4446.
[9] M.A. Fernandez-Yague, D. Pastorino, E.B. Montufar, C. Canal, M. Manzanares-Cespedes, M.P. Ginebra, In Vivo Efficiency of Antimicrobial Inorganic Bone Grafts in Osteomyelitis Treatments, Materials Science and Engineering: C, 2019.
[10] R.M.Y. Wong, T.-k. Li, J. Li, W.-T. Ho, S.K.H. Chow, S.S.Y. Leung, W.-H. Cheung, M. Ip, A systematic review on current osteosynthesis-associated infection animal fracture models, J. Orthop. Transl. 23 (2020) 8–20.
[11] Y.H. An, Q.K. Kang, C.R. Arciola, Animal models of osteomyelitis, Int. J. Artif. Organs 29 (4) (2006) 407.
[12] L. Scheman, M. Janota, P. Lewin, The production of experimental osteomyelitis: preliminary report, JAMA 11 (18) (1941) 1525–1529.
[13] C.W. Norden, R.L. Myerowitz, E. Keleti, Experimental osteomyelitis due to Staphylococcus aureus or Pseudomonas aeruginosa: a radiographic-pathological correlative analysis, Br. J. Exp. Pathol. 61 (4) (1980) 451.
[14] D.P. Clark, C.T. Badea, Advances in micro-CT imaging of small animals, Phys. Med. 88 (2021) 175–192.
[15] J. Horn, U. Schlegel, C. Krettek, K. Ito, Infection resistance of unreamed solid, hollow slotted and cannulated intramedullary nails : an in-vivo experimental comparison, J. Orthop. Res. 23 (4) (2010) 810–815.
[16] R. Salman, M. Mcgraw, L. Naffaa, Chronic osteomyelitis of long bones: imaging pearls and pitfalls in pediatrics, Seminars Ultrasound, CT MRI (4) (2021).
[17] T.A. Freeman, P. Patel, J. Parvizi, V. Antoci, I.M. Shapiro, Micro-CT analysis with multiple thresholds allows detection of bone formation and resorption during ultrasound-treated fracture healing, J. Orthop. Res. 27 (5) (2010) 673–679.
[18] H. Bolotin, DXA in vivo BMD methodology: an erroneous and misleading research and clinical gauge of bone mineral status, bone fragility, and bone remodelling, Bone 41 (1) (2007) 138–154.
[19] S. Nuzzo, M.H. Lafage-Proust, E. Martin-Badosa, G. Boivin, T. Thomas, C. Alexandre, F. Peyrin, Synchrotron radiation microtomography allows the analysis of three-dimensional microarchitecture and degree of mineralization of human iliac crest biopsy specimens: effects of etidronate treatment, J. Bone Miner. Res. 17 (8) (2002).
[20] A. Wenaden, T.A. Szyszko, A. Saifuddin, Imaging of periosteal reactions associated with focal lesions of bone, Clin. Radiol. 60 (4) (2005) 439–456.
[21] L.Y. Jin, S. Sufi, M. Kshitij, K. Nikhil, R. Gajan, The imaging of osteomyelitis, Quant. Imag. Med. Surg. 6 (2) (2016) 184.
[22] D. Jaramillo, Infection: musculoskeletal, Pediatr. Radiol. 41 (s1) (2011) S127.
[23] J.C. Odekerken, J.J. Arts, D.A. Surtel, G.H. Walenkamp, T.J. Welting, A rabbit osteomyelitis model for the longitudinal assessment of early post-operative implant infections, J. Orthop. Surg. Res. 8 (1) (2013) 38.
[24] A. Mescher, N. York, C. San, F. Athens, L. Madrid, M. City, Junqueira's Basic Histology, fifteenth ed., 2018.
[25] G.M. Caputo, P.R. Cavanagh, J.S. Ulbrecht, G.W. Gibbons, A.W. Karchmer, Assessment and management of foot disease in patients with diabetes, N. Engl. J. Med. 331 (13) (1994) 854–860.
[26] L.E. Jauregui, C.L. Senour, Diagnosis and Management of Bone Infections, M. Dekker, 1995.
[27] Y. Yang, L. Liu, H. Luo, D. Zhang, K. Zhou, Dual-purpose magnesium-incorporated titanium nanotubes for combating bacterial infection and ameliorating osteolysis to realize better osseointegration, ACS Biomater. Sci. Eng. 5 (10) (2019).
[28] J. Li, J. Wang, D. Wang, G. Guo, K. Yeung, X. Zhang, X. Liu, Band gap engineering of titania film through cobalt regulation for oxidative damage of bacterial respiration and viability, Compendex 9 (33) (2017) 27475–27490.
[29] I. Qayoom, A.K. Teotia, A. Panjla, S. Verma, A. Kumar, Local and sustained delivery of rifampicin from a bioactive ceramic carrier treats bone infection in rat tibia, ACS Infect. Dis. 6 (11) (2020) 2938–2949.
[30] S. Zhang, G. Chen, M. Wang, B. Lin, X. Gao, J. Hu, B. Chen, C. Zhang, Osteogenic and anti-inflammatory potential of oligochitosan nanoparticles in treating osteomyelitis, Mater. Sci. Eng. C (2022), 112681.
[31] C. Pineda, R. Espinosa, A. Pena, Radiographic imaging in osteomyelitis: the role of plain radiography, computed tomography, ultrasonography, magnetic resonance imaging, and scintigraphy, Semin. Plast. Surg. 23 (2) (2009) 80–89.

[32] A. Nasser, T. Azimi, S. Ostadmohammadi, S. Ostadmohammadi, A comprehensive review of bacterial osteomyelitis with emphasis on Staphylococcus aureus, Microb. Pathog. 148 (2020), 104431.
[33] H.K. Vaananen, T. Laitala-Leinonen, Osteoclast lineage and function, Arch. Biochem. Biophys. 473 (2) (2008) 132–138.
[34] M.J. Bossard, T.A. Tomaszek, S.K. Thompson, B.Y. Amegadzie, M.A. Levy, Proteolytic activity of human osteoclast cathepsin K. Expression, purification, activation, and substrate identification, J. Biol. Chem. 271 (21) (1996) 12517–12524.
[35] J.A. Wright, S.P. Nair, Interaction of staphylococci with bone, Int. J. Med. Microbiol.: IJMM 300 (2-3) (2009) 193–204.
[36] Y. Han, X. You, W. Xing, Z. Zhang, W. Zou, Paracrine and endocrine actions of bone——the functions of secretory proteins from osteoblasts, osteocytes, and osteoclasts, Bone Res. (2018).
[37] C.E. Decamp, Brinker, Piermattei and Flo's Handbook of Small Animal Orthopedics and Fracture Repair || Fractures of the Pelvis, 2016, pp. 437–467.
[38] A. Nemec, M.J. Lommer, S.M. Marretta, Management of maxillofacial osteonecrosis, in: Oral and Maxillofacial Surgery in Dogs and Cats, 2020.